ACS OMEGA

Open Access

http://pubs.acs.org/journal/acsodf

Article

Experimental Study on Enhanced Methane Detection Using an MEMS-Pyroelectric Sensor Integrated with a Wavelet Algorithm

Wei Dong,* Yuichi Sugai,* Yongjun Wang, Hemeng Zhang, Xiaoming Zhang, and Kyuro Sasaki

Cite This: *ACS Omega* 2024, 9, 19956−19967

Read Online

ACCESS | Metrics & More | Article Recommendations

ABSTRACT: An optical sensing approach that balances portability with cost efficiency has been designed for the reliable monitoring of fugitive methane (CH_4) emissions. Employing a $LiTaO_3$-based pyroelectric detector integrated with micro-electro-mechanical systems and a broad infrared source, the developed gas sensor adeptly measured CH_4 concentrations with a low limit of detection of about 5.6 ppm_v and showed rapid response times with t_{90} consistently under 3 s. Notably, the novelty of our method lies in its precise control and reduction of CH_4 levels, enhanced by wavelet denoising. This technique, optimized through meticulous grid search, effectively mitigated noise interference noticeable at CH_4 levels below 10 ppm_v. Postdenoising, nonlinear regression analyses based on the modified Beer−Lambert equation returned R^2 values of 0.985 and 0.982 for the training and validation sets, respectively. In conclusion, this gas sensor has been shown to be able to meet the requirements for early warning of CH_4 leakage on the surface in various carbon capture, utilization, and storage projects such as enhanced oil or gas recovery projects using CO_2 injection.

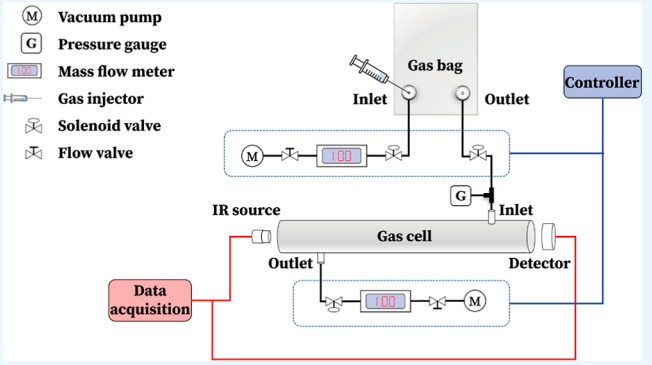

INTRODUCTION

Methane (CH_4), as a potent greenhouse gas, warrants attention because of its significant global warming effect compared to carbon dioxide (CO_2).[1−3] Recent data shows a concerning surge in global atmospheric CH_4 levels since 2007, with a marked increase from 2014.[4] Concurrently, with governments increasingly focusing on CO_2 issues and the maturation of carbon capture, utilization, and storage (CCUS) technologies,[5−7] breakthroughs have been achieved in practical applications like CO_2-enhanced oil recovery (CO_2-EOR), coal bed methane (CO_2-ECBM), and shale gas (CO_2-ESG). However, the high pressures required to achieve supercritical CO_2 injection states might inadvertently heighten the risk of natural gas (predominantly CH_4) leakages, potentially jeopardizing adjacent ecosystems and communities.

Oil and gas operations are responsible for a significant portion of increased CH_4 in the atmosphere.[8,9] Considering the declared environmental and climate impacts, monitoring CH_4 emissions from the surface to the atmosphere in traditional oil and gas operations as well as in emerging CCUS project development is critical. Achieving precise detection and quantification of CH_4, especially at low concentrations of less than 10 ppm, remains a challenge. Beyond accuracy, the need for miniaturization and ease of deployment are crucial, particularly given the vast and varied characteristics of oil and gas fields. While methods like gas chromatography and mass spectrometry are known for their precision,[10,11] their high cost and operational complexities can restrict their widespread adoption for continuous leakage monitoring.

Optical sensing technologies, however, are emerging as promising tools for precise CH_4 measurement in the context of CCUS. Technologies such as wavelength modulation spectroscopy (WMS), when combined with approximation methods, have shown enhanced sensitivity and resolution, effectively mitigating issues of spectral line interference at atmospheric pressure.[12−17] The study by Xia et al. (2021) demonstrated that WMS, supplemented with Allan deviation analysis, could detect CH_4 concentrations as low as 560 ppt, with a 290 s averaging time.[13] Furthermore, other absorption spectroscopy-based optical methods such as tunable diode laser absorption spectroscopy,[18,19] cavity ring-down spectroscopy,[20,21] cavity enhanced absorption spectroscopy,[22] quartz-enhanced photoacoustic spectroscopy,[23,24] Fourier transform infrared spectroscopy,[25,26] and off-axis integrated cavity output

Received: December 7, 2023
Revised: January 31, 2024
Accepted: February 9, 2024
Published: April 26, 2024

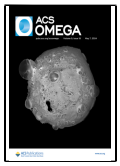

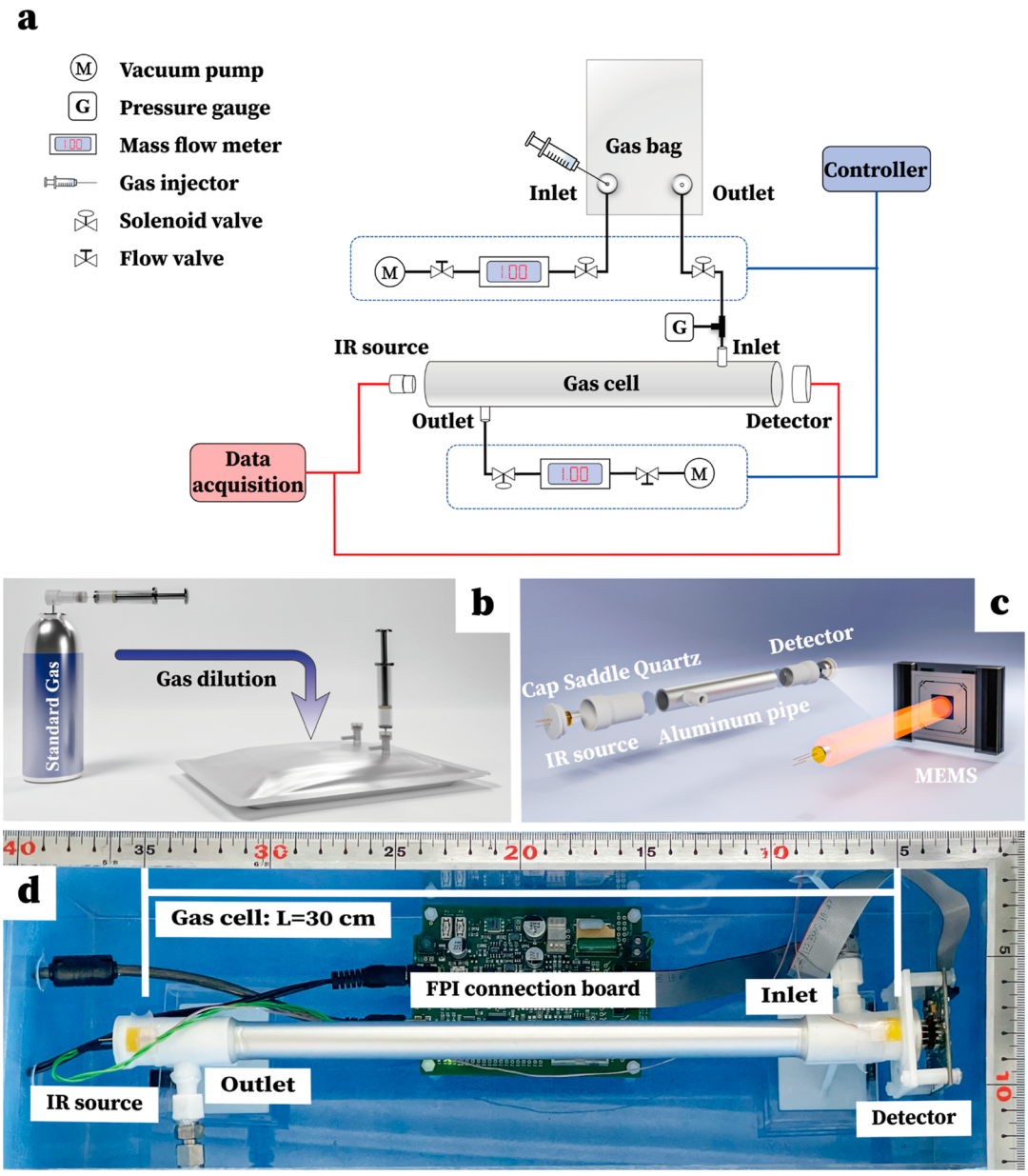

Figure 1. (a) Schematic representation of the experimental setup, detailing the control unit and data acquisition methodology. (b) Illustration of gas sample preparation at varying concentrations and the associated dilution process. (c) Exploded view detailing the internal components of the gas cell. (d) Photograph of the gas sensor assembly, highlighting the gas cell length of ~30 cm.

spectroscopy[27−29] have been employed for CH_4 measurements.

However, their practical application has been limited due to the necessity of sophisticated optical components and high associated costs, confining their use predominantly to scientific research.[30] On the other hand, the integration of micro-electro-mechanical system (MEMS) detectors with infrared (IR) sources has paved the way for the development of compact, low-power, and cost-effective gas sensors for CO_2 monitoring.[31−38] Despite this progress, there is a paucity of such advancements in the field of low-concentration CH_4 detection.

To address this challenge, our study presents an optical sensing device that balances simplicity with high reliability for the detection of low-concentration CH_4 emissions. The device incorporates a MEMS-based pyroelectric detector, which is designed to achieve a low limit of detection, thereby facilitating early warning of CH_4 leakages at the surface. Additionally, the impact of environmental changes, such as temperature fluctuations, on the accuracy of CH_4 detection is examined. To further enhance the limit of detection for CH_4, a wavelet denoising technique is employed to overcome the issue of an insufficient signal-to-noise ratio (SNR). This additional step enhances the CH_4 detection limit for CCUS production operation safety, moving us closer to a more sustainable and carbon-neutral future.

EXPERIMENTAL SECTION

Comprehensive Experimental Design for CH_4 Spectrometry. In this work, the comprehensive experimental design for CH_4 spectrometry, which comprises the experimental layout and approach, is systematically presented and illustrated in Figure 1. Presented in Figure 1a is the experimental design schematic specifically customized for

https://doi.org/10.1021/acsomega.3c09769
ACS Omega 2024, 9, 19956−19967

CH_4 measurement, integrating both a spectrally tunable pyroelectric detector and a thermal IR source to offer a comprehensive solution for accurate gas detection. Two vacuum pumps, each capable of a maximum flow rate of 12 L/min, supply the essential gas flow momentum. Furthermore, these pumps can swiftly create and sustain a vacuum, given a negative pressure of at least 0.062 MPa. High-precision needle valves from Swagelok are attached to the pumps' outlets or inlets to ensure rigorous flow regulation. Each mass flow meter, calibrated for a 0 to 1 L/min range, continuously monitors the flow rate of both the incoming and outgoing gas. Throughout the experiment, this flow rate is consistently held at 1 L/min with a tolerance of ±0.01 L/min.

Gas samples were housed within an aluminum foil sampling bag, with solenoid valves positioned at both the inlet and outlet to safeguard against potential contamination. Figure 1b illustrates the primary gas dilution procedure, which employs a high-precision microsyringe as the standard gas injector. It administered 1 mL of 99.9% pure CH_4, provided by GL Sciences, into the sampling bag. Conducted under indoor ambient atmospheric conditions at ∼26 °C, the injection was followed by the introduction of a meticulously measured 1000 mL volume of ambient air, regulated by a mass flow meter and controller, yielding an initial CH_4 concentration of 1000 ppm_v.

Absorption spectrometry measurements were performed using a custom-made aluminum alloy gas cell with a length of ∼30 cm, translating to an estimated internal volume of ∼46.2 mL as shown in Figure 1c. It was designed with specialized saddles and caps, created using advanced 3D printing technology, to precisely fit the unique dimensions of both the detector and IR source. To ensure consistent gas flow and maintain airtightness in the MEMS, both ends of the gas cell were fitted with ultratransparent quartz sheets, which were secured with a resilient silicone-based adhesive that also anchored the cell to the saddles and sealed the connectors at both the inlet and outlet. Moreover, the gas cell's port features solenoid valves to prevent gas leakage and contamination, and a pressure gauge allows real-time monitoring of the internal gas pressure.

Data acquisition was achieved using a Fabry−Pérot interferometer (FPI) connection board as shown in Figure 1d. This board was integrated with a $LiTaO_3$-based pyroelectric detector equipped with Fabry−Pérot filters, specifically the LFP-3144C-337 model from InfraTec, which operated effectively within the spectral range of 3100−4400 nm. Complementing this setup was the IR emitter EMIRS200 from Axetris, which emitted wavelengths ranging from 2 to 14 μm. The FPI connection board was then connected to a PC via a USB cable, facilitating the configuration of operating parameters and relaying measurement data through specialized software (FPI Evaluation Workbench) on the computer. Additionally, the gas sensor was housed within a box that is 40 cm long, enhanced with insulation layers to bolster temperature stability. Two surface-mount thermocouples gauged the temperature at the gas cell's extremities, while a probe-type thermocouple assessed the ambient temperature.

Optical Configuration of the MEMS-Integrated Fabry−Pérot Filter. Fabry−Pérot filters, consisting of two parallel reflective surfaces, form an optical cavity. When integrated with MEMS technology, these filters produce interference patterns that enable the selective transmission of specific light wavelengths. Ebermann et al. (2016) demonstrate the mechanical design of the MEMS structure for the filter, where the integration of T-shaped spring suspensions as stress-relief components is specifically aimed at optimizing the efficiency of wavelength selection. Made from $LiTaO_3$ and housed within a TO-8 package, the pyroelectric detector is strategically positioned at the output end of the Fabry−Pérot filter for effective gas sensing, with a detailed design breakdown available in ref 39.

Neumann et al. (2009) illustrate the cross section of the optical cavity.[40] The distance between the reflective surfaces can be modulated using control electrodes. This precise modulation of the cavity distance is achieved using the FPI Evaluation Workbench software suite, facilitating interference-based wavelength selection. By regulating the cavity length, specific wavelengths of light can be selected and filtered effectively for pyroelectric sensing elements. The associated technology of the Fabry−Pérot filter offers notable advantages, including high precision, compactness, and energy efficiency, rendering it a highly reliable solution for optical filtering.

Automated Control of CH_4 Gas Mixture Concentrations. To achieve varying concentrations of the CH_4 gas mixture, precise control over the volume of diluent-air intake at a specific flow rate was imperative. This control was executed by a system board centered around the STM32F407ZGT6 microcontroller, which acted as a dedicated gas mixture controller in line with eq 1. The precision process began with the manual injection of a set volume of pure CH_4 standard gas. Subsequent concentrations were then autonomously determined using the pre-established dilution factor α, reducing potential operational inaccuracies associated with manual gas handling. The microcontroller, with its sophisticated timer, managed the activation intervals of the solenoid valve and pump, ensuring meticulous control throughout the gas sample dilution phase.

$$C_{\text{mixture}} = \sum (-\alpha)\frac{V_{CH_4}}{V_{\text{air}}}, \qquad \alpha \in (0, 1) \tag{1}$$

where C_{mixture} denotes the gas sample concentration and α represents the dilution factor governing the extraction volume, while V_{CH_4} and V_{air} are the initial volumes of CH_4 and air, respectively.

Our methodology initially introduced 1 mL of pure CH_4 into the gas bag depicted in Figure 1b. The controller managed the gas bag filling at a flow rate of 1 L/min, resulting in a CH_4 concentration of 1000 ppm_v after a 1 min air injection. With the dilution factor α set to 0.25, it signifies that at a flow rate of 1 L/min, one-quarter of the sample gas within the gas bag is discharged. Simultaneously, an equivalent volume of fresh air is introduced. This series of actions leads to a gradual reduction in CH_4 concentration, reaching 1 ppm_v after 25 consecutive dilutions.

The present experiments were conducted in a laboratory specifically engineered for superior air circulation. Leveraging an efficient air conditioning system, we ensured that the circulating air maintained a stable ambient temperature, consistently around ∼26 °C. While the ambient air, used as the diluent, naturally encompasses minute traces of CH_4, these minor fluctuations in concentration were deemed negligible for the purposes of our study. As detailed in Table 1, the final concentration distribution, which emitted a group of signal responses from the detector, was derived from these dilution steps and served as the foundational data set for the rigorous performance evaluation of the gas sensor.

https://doi.org/10.1021/acsomega.3c09769
ACS Omega 2024, 9, 19956−19967

Table 1. Evolution of CH_4 Gas Concentration Dilution

cycle	CH_4 (mL)	air (mL)	conc. (ppm_v)
1	1.0000	1000	1000.0
2	0.7500	1000	750.0
3	0.5625	1000	562.5
4	0.4219	1000	421.9
5	0.3164	1000	316.4
6	0.2373	1000	237.3
7	0.1780	1000	178.0
8	0.1335	1000	133.5
9	0.1001	1000	100.1
10	0.0751	1000	75.1
11	0.0563	1000	56.3
12	0.0422	1000	42.2
13	0.0317	1000	31.7
14	0.0238	1000	23.8
15	0.0178	1000	17.8
16	0.0134	1000	13.4
17	0.0100	1000	10.0
18	0.0075	1000	7.5
19	0.0056	1000	5.6
20	0.0042	1000	4.2
21	0.0032	1000	3.2
22	0.0024	1000	2.4
23	0.0018	1000	1.8
24	0.0013	1000	1.3
25	0.0010	1000	1.0

Stratified Sampling for Improved Nonlinear Regression Analysis. In our investigation, we observed a clear skewness in the distribution of the sampled data,[41] which was not consistent with a desirable uniform or random pattern. The presence of this nonuniformity complicates nonlinear regression analyses, specifically when dense data clustering in certain intervals leads to model overfitting. Consequently, the model's predictive accuracy can be compromised in sparser data regions. Analyzing the data set with the probability density function[42,43] as shown in eq 2, we identified a significant concentration of data at the lower-concentration boundaries. Such skewed distributions can limit model adaptability and interpretability. Recognizing these challenges, it is crucial to leverage techniques like stratified sampling to achieve a more balanced data representation, fortifying the robustness of subsequent analyses and interpretations.

$$P(1 < X < 1000) = \int_1^{1000} f(d)\mathrm{d}x \tag{2}$$

For our stratified sampling approach, we demarcated the concentration range into three distinct intervals using four boundaries: 1000, 300, 10, and 1 ppm_v. Within these strata, three samples were systematically acquired, summing to nine primary data points. Recognizing 1000 and 1 ppm_v as pivotal benchmark concentrations, we integrated them directly into the data set, bringing the total data count to 11. Figure 2 shows the poststratification sample distribution, which was further divided into two data sets: one for training the regression model and the other for validation purposes. Given the objective emphasis on low-concentration CH_4 detection, the sampling technique inherently leans toward these lower-concentration regions.

Addressing Sensitivity and Noise with Grid Search Wavelets. We chose the high-resolution method primarily for its superior sensitivity in differentiating CH_4 signal responses across varied concentrations. However, such heightened sensitivity also inadvertently amplified noises from sources like mechanical vibrations, ambient temperature fluctuations, and electrical interferences.[44−46] Pyroelectric detectors were particularly adept at capturing rapid temperature changes. Yet, their dual pyroelectric and piezoelectric properties made them susceptible to microphonic effects.[31] Mechanical stresses and electromagnetic interferences during system operation further exacerbated the noise challenges. To address this intricate challenge of distinguishing genuine signals from noise, we adopted the PyWavelets package[47] to develop a parameter optimization model, with both parameters and methods finely tuned via grid search, as detailed in Table 2. For denoising discrete signals in the time domain using three types of wavelets: Daubechies (db), Symlets (sym), and Coiflets (coif), we set the window size from 2 to 12 with a step of 2, levels from 1 to 7 with a step of 1, and a threshold ranging from 0.1 to 0.7 with a step of 0.1 as our base parameters.

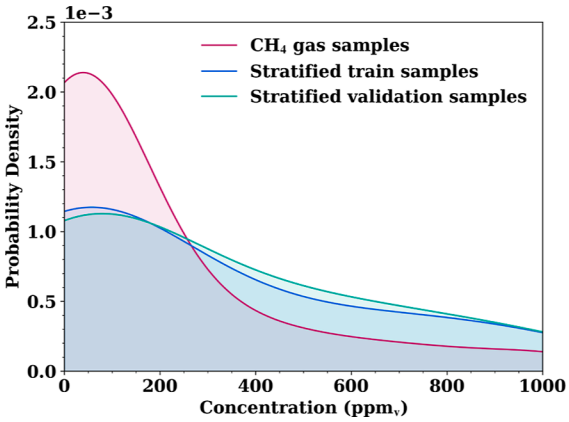

Figure 2. Distribution of CH_4 gas samples highlighting the enhanced balance achieved through stratified sampling with an emphasis on lower-concentration regions.

Table 2. Grid Configuration for Wavelet Parameters Search

wavelet type	window size	level	thresholds
dB sym coif	2 to 12, step = 2	1 to 7, step = 1	0.1 to 0.7, step = 0.1

Navigating the complexities of our chosen method's heightened sensitivity required a robust noise reduction approach. Drawing parallels between wavelet denoising and grid search provided a comprehensive framework. As we measured the quality of a denoised signal using metrics such as energy preservation (E) in eq 3, mean squared error (MSE) in eq 4, and peak SNR (PSNR) in eq 5,[48−50] we were reminded of how wavelet parameter performance was quantified. Through this lens, our commitment to isolating precise CH_4 signature signals amidst the persistent challenges of system noise became evident.

$$E = \sum_{t=1}^{N} |x(t)|^2 \tag{3}$$

where $x(t)$ represents the signal amplitude at time t, and N is the total sample count.

https://doi.org/10.1021/acsomega.3c09769
ACS Omega 2024, 9, 19956−19967

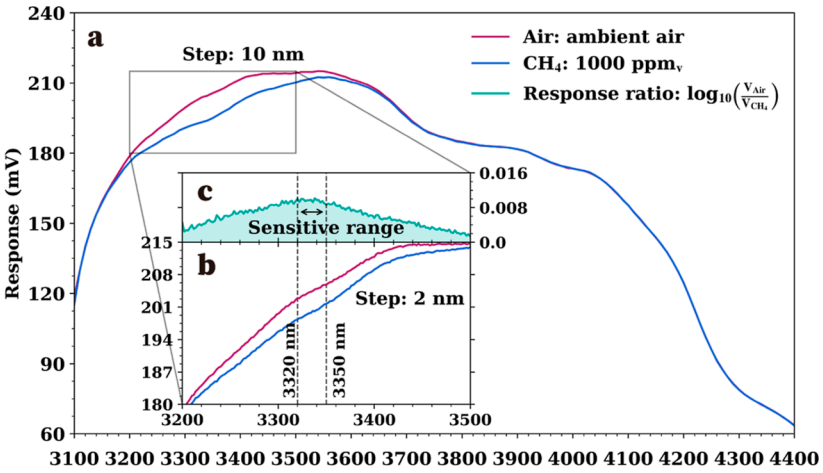

Figure 3. Selection of sensitivity wavelength for CH_4 detection: (a) 10 nm scan step used to determine the initial range of wavelengths sensitive to CH_4 detection, (b) refinement of the wavelength scan using a 2 nm step, enhancing precision in identifying wavelengths with heightened CH_4 detection sensitivity, and (c) response of measurements distinguishing between air and CH_4, providing valuable insights into variations in the system output,.

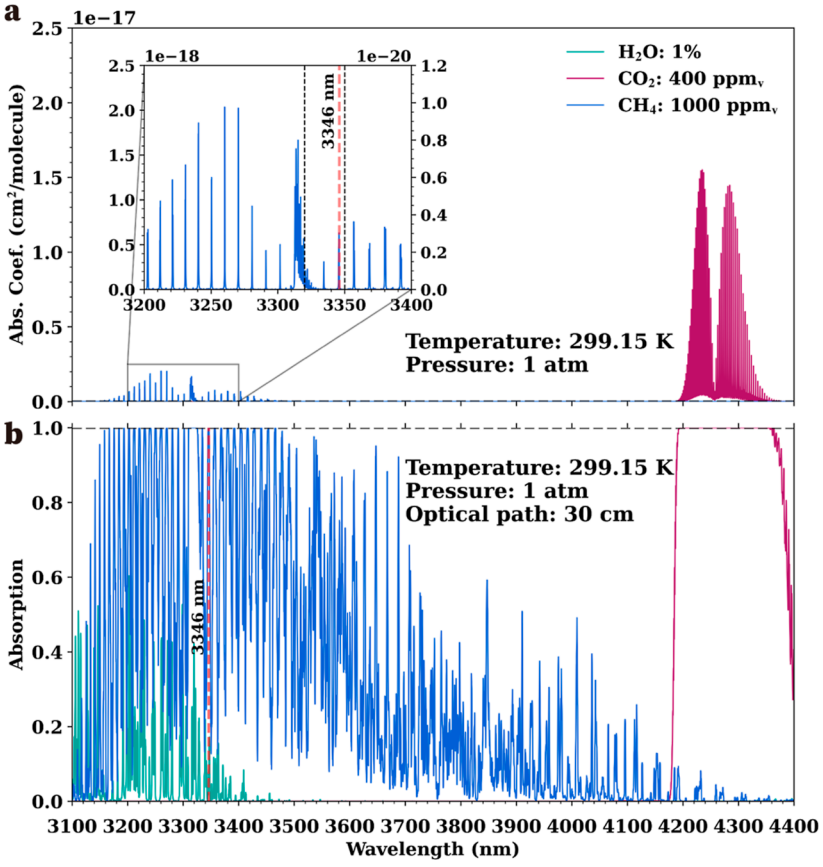

Figure 4. Simulation from the HITRAN database: (a) absorption coefficients of H_2O, CO_2, and CH_4 using data from the HITRAN database, inset highlights the most sensitive region for CH_4, leading to the initial selection of 3346 nm as the optimal wavelength and the (b) absorption spectrum of H_2O, CO_2, and CH_4 at 299.15 K and 1 atm, using an optical path length of 30 cm.

$$\mathrm{MSE} = \frac{1}{N}\sum_{t=1}^{N}[x(t) - \hat{x}(t)]^2 \tag{4}$$

where $x(t)$ and $\hat{x}(t)$ are the original and denoised signals at time t, respectively.

$$\mathrm{PSNR} = 10\cdot\log_{10}\left(\frac{\mathrm{MAX}^2}{\mathrm{MSE}}\right) \tag{5}$$

where MAX is the peak amplitude of the original signal.

RESULTS AND DISCUSSION

Experimental and Simulation Insights for Sensitive Wavelength. In our effort to determine the most suitable

https://doi.org/10.1021/acsomega.3c09769
ACS Omega 2024, 9, 19956−19967

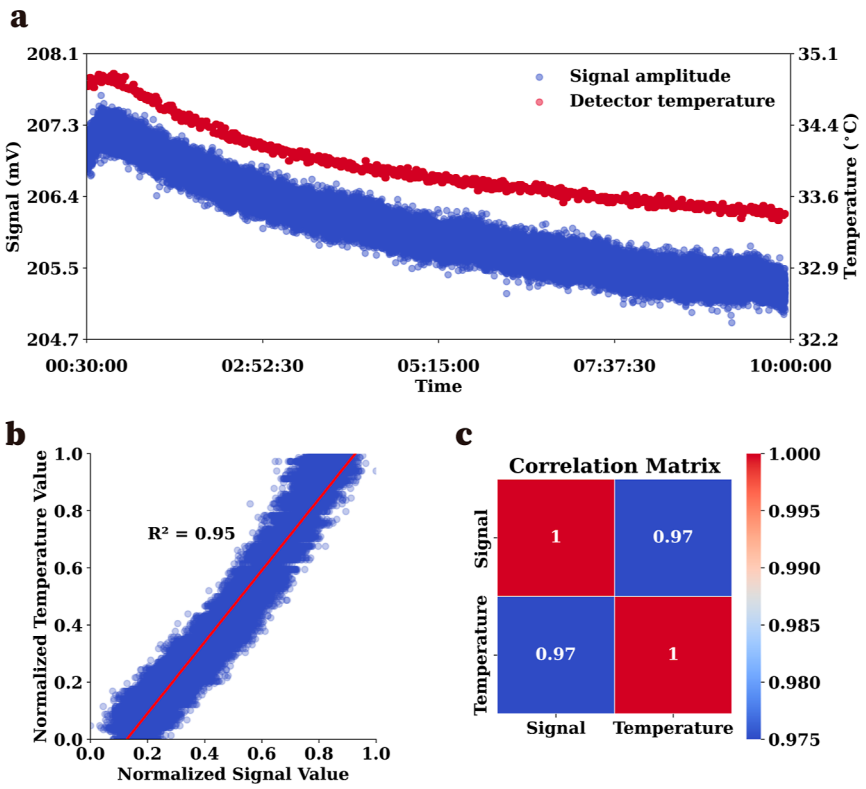

Figure 5. Temperature effects on the detector's signal response: (a) signal variation corresponding to temperature change with an evident increase during the manual temperature rise and a subsequent decrease, (b) linear fit between normalized signal and temperature values, showing a consistent relationship with R^2 = 0.95, and (c) correlation matrix between signal values and temperature, indicating a strong correlation with a Pearson coefficient of 0.97.

wavelength for CH_4 detection, we used two distinct scanning steps as shown in Figure 3. Initiating with a 10 nm step size, we conducted a broad scan across the 3100 to 4400 nm wavelength range, which not only facilitated rapid scanning but also identified a preliminary CH_4 response window between 3200 and 3500 nm as shown in Figure 3a.

For enhanced resolution, we then proceeded with a finer 2 nm step size, focusing specifically on the initially identified window. Figure 3b shows a detailed view of this region, and as a result, a sensitive range of 3320 to 3350 nm was delineated, further highlighted in Figure 3c. This specific range was determined by comparing the response ratio (RespR) of the reference voltage V_{air}, measured from ambient air, to the voltage V_{CH_4} obtained from a CH_4 concentration of 1000 ppm_v, as described in eq 6

$$\text{response ratio} = \log_{10} \frac{V_{\text{reference}}}{V_{\text{target}}} \tag{6}$$

where response ratio is the logarithm of the ratio between the voltage representation of the measured target and the reference voltage, $V_{reference}$ represents the voltage at the reference point, and V_{target} means the voltage value at the gas sample measurement point.

Identifying the optimal wavelength for CH_4 detection within the sensitive range proved to be challenging due to minor variations in that domain. Determining the root causes of these slight differences, whether attributed to noise interference or other variables, presents a challenge. To address this complexity, we turned to HAPI data from the HITRAN database.[51] By simulating and analyzing the absorption coefficient and rate of CH_4, and considering its main interference sources, CO_2 and H_2O, under specific conditions, we were able to offer a clearer evaluation.

Figure 4a shows the absorption coefficient simulation for 1% H_2O, 400 ppm_v CO_2, and 1000 ppm_v CH_4 at 299.15 K and 1 atm in the wavelength range of 3100 to 4400 nm, which matches our experimental conditions closely. The data highlight a distinct absorption coefficient for CH_4 in the 3200 to 3400 nm region, with minimal interference from CO_2. The inset magnifies the absorption features of CH_4 and H_2O, pointing to 3346 nm as the ideal wavelength due to its strong absorption coefficient. Even though there is a potential influence from H_2O, the discrepancy is on the order of 10^3, making it minor and manageable through the use of desiccants. Figure 4b confirms the dominant absorption rate of CH_4 at 3346 nm compared to H_2O under the given conditions with an optical path of 30 cm. In our experiments conducted at a single wavelength of 3346 nm, we evaluated the detector's capability in quantifying various CH_4 concentrations within a controlled lab setting, spanning conditions from vacuum to air and mixes of CH_4 and air.

Exploring the Thermal Sensitivity of the Pyroelectric Detector. The pyroelectric detectors, while excellent at capturing rapid temperature fluctuations, exhibit vulnerability to microphonic effects due to their inherent pyroelectric and piezoelectric properties, as highlighted by Ng et al.[31] To understand the temperature effects on the detector's performance and validate our findings, we conducted an extensive laboratory test on static air under natural conditions for nearly 10 h. In our pursuit of minimizing perturbations stemming from human activities, the experimental window was

https://doi.org/10.1021/acsomega.3c09769
ACS Omega 2024, 9, 19956−19967

judiciously selected to span from 00:30:00 to 10:00:00. The procedural commencement was marked by a 30 min interval of deliberate temperature escalation, subsequently giving way to a period of natural temperature diminution within the confines of a deserted laboratory setting, a strategic move aimed at deciphering the resultant modulations in the detector signal.

Elucidated in Figure 5, the experimental outcomes offer a comprehensive visual narrative. Figure 5a simultaneously illustrates both the temperature dynamics and the signal's trajectory, highlighting an ascending signal with increasing temperature and a subsequent descent, while maintaining an almost invariant peak-to-peak signal magnitude, thereby demonstrating the intricate interplay between temperature and signal behavior.

Progressing to a quantitative analysis, we engaged in a linear fitting exercise postnormalization of signal and temperature values, the results of which are presented in Figure 5b. This exercise culminated in the revelation of a strong, linear correlation between the signal values and temperature, a fact underscored by a coefficient of determination (R^2) value of 0.95, signaling a high degree of concordance. The exploration reached its peak with the construction of a correlation matrix between signal values and temperature, shown in Figure 5c. Here, a Pearson correlation coefficient of 0.97 emerged, testifying to an exceptionally strong interdependence.

In the comprehensive statistical analysis presented in Table 3, the signal response is characterized by an average value of

Table 3. Statistical Description of the Signal Response, Temperature of the Detector, and Peak-To-Peak Voltage

statistic	signal response (mV)	detector (°C)	peak-to-peak voltage (mV)
mean	206.027	33.9	0.111
std	0.554	0.4	0.084
min	204.893	33.4	0
25%	205.560	33.6	0.044
50%	205.910	33.8	0.093
75%	206.415	34.2	0.160
max	207.618	34.9	0.733

206.027 mV. The median settles at 205.910 mV, oscillating between 204.893 and 207.618 mV. As for the temperature of the detector, observations yield an average of 33.9 °C, with a span from 33.4 up to 34.9 °C; the median is consistently at 33.8 °C. Particularly noteworthy is the fact that the peak-to-peak voltage demonstrates an average of 0.111 mV, with its median registering closely at 0.093 mV. This suggests a commendable stability and symmetry in the signal response distribution. However, the maximum value of 0.733 mV also indicates that certain sample points might have been influenced due to outliers or noise interference.

High-Resolution Performance of CH_4 Gas Detection. Figure 6 shows the raw CH_4 signal captured through a cyclic measurement method with intervals of 45 s across 25 cycles, spanning CH_4 concentrations from 1000 to 1 ppm_v. Due to the detector's 60 s temperature compensation cycle, there are periods without data acquisition, leading to observable gaps in the collected data. To mitigate this, we divided and regrouped the data indicated by the dotted line in Figure 6a. In our assessment of the gas sensor's response times for identifying CH_4 within mixtures at concentrations of 100.1 and 75.1 ppm_v, we found that the t_{90} value—representing the duration for the sensor's signal to reach 90% of its final value—was less than 3 s as shown in Figure 6b. Such a rapid response surpasses many existing studies and underlines the sensor's potential for timely and accurate detection in critical scenarios associated with CCUS projects. When analyzing the segmented data using the box plot method, the maximum values from each group exhibited a distinct linear pattern. In contrast, the trend of the minimum values is consistent with the Beer−Lambert law as shown in Figure 6c. The peak and base values within each segment represent the voltage responses for the vacuum state and the varying CH_4 concentrations, respectively.

Upon examining the gas sensor's precision in detecting ambient air through five repeated tests, we used the peak voltage response $V_{reference}$ in a vacuum and the lowest V_{air} during ambient air inflow to the gas cell to determine the air RespR based on eq 6. As shown in Figure 6d, our measurements yielded an average response ratio of 1.182×10^{-3} with a variation of $\pm 7.24 \times 10^{-5}$. It indicates that the CH_4 in ambient air, essentially representing a baseline with a net CH_4 concentration of 0 ppm_v in the air mixture, produces a value nearly equivalent to this ratio. Notably, this value is slightly less than the 1.225×10^{-3} RespR observed when air is mixed with a net content of 1 ppm_v of CH_4, highlighting the sensor's refined sensitivity to CH_4 gas.

While Figure 6 demonstrated the gas sensor's impressive ability to detect CH_4 concentrations ranging from 1000 to 1 ppm_v, highlighting the advantages of the high resolution, it also revealed certain drawbacks. The simplified design of the gas sensor, although efficient and of low cost, seemed to be more susceptible to interference, resulting in notable signal deviations. This issue became particularly noticeable for CH_4 concentrations below 10 ppm_v, where we observed an increase in voltage inconsistencies, affecting signal precision. Given the design's inherent simplicity, reducing noise through structural changes appeared challenging. Therefore, the need for a strong noise reduction algorithm became evident to enhance signal quality.

Tuning Wavelet Parameters for Robust CH_4 Sensing. Wavelet denoising is a sophisticated method whose performance is intricately tied to the selection of its parameters. Our approach to understanding this entailed a deep dive into three primary metrics: E, MSE, and PSNR. Figure 7a shows how wavelet levels critically influence denoising. Across all wavelet types, E scores rise with increased window sizes and levels. The "coif" wavelet, in particular, exhibits superior performance. However, while the MSE rises with these increments across all types, the distinctions are minimal. Conversely, the PSNR score declines with increased levels, showing a similar pattern across different wavelet types.

Turning to Figure 7b which highlights the influence of thresholds, we observed that an increase in thresholds only slightly affects the E scores. It is only when the window size grows that these values rise, with the "coif" wavelet standing out again. The changes in MSE and PSNR due to threshold variations are similar to those caused by different levels in both scale and trend. These observations emphasize that balanced levels and thresholds are essential to achieving the finest denoising results while larger window sizes have clear advantages.

While the "coif" wavelet clearly outperforms the "db" and "sym" in terms of E scores, relying solely on one metric can be misleading. Overaggressive denoising might eliminate most of the intricate details, yielding an impressive score but compromising data fidelity. Therefore, our next step involves

https://doi.org/10.1021/acsomega.3c09769
ACS Omega 2024, 9, 19956−19967

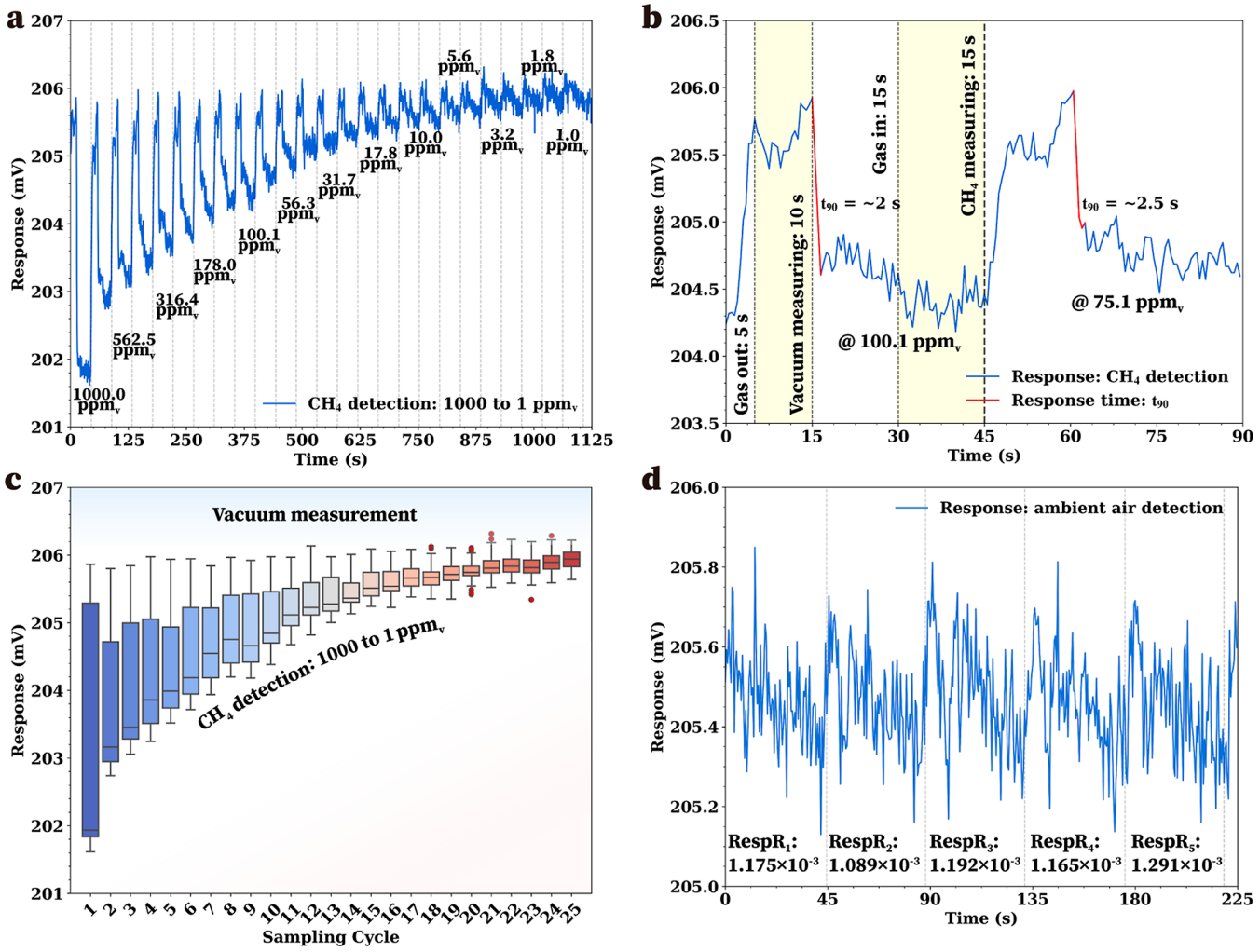

Figure 6. Gas-specific signal response measurements: (a) signal response during CH_4 measurements transitioning between a vacuum state and CH_4 gas at 45 s intervals, (b) evaluation of t_{90} response time for the gas sensor when detecting 100.1 and 75.1 ppm_v CH_4 mixtures, (c) box plot representation of voltage variations across the cycles, and (d) depiction of the signal response of the gas sensor to indoor ambient air.

a regression analysis using the modified Beer−Lambert equation as detailed in eq 7.[31,52] We determined the optimal parameter selection based on the R^2 values. Upon analyzing our stratified-sampled training data, we identified that using the wavelet type "sym", a window setting of "10", level "6", and threshold "0.4" resulted in an optimal R^2 value of 0.985, indicating an exceptionally strong regression effect for these parameters in our model. Furthermore, the result demonstrates that while the "coif" wavelet clearly outperforms others, it might be a consequence of overaggressive denoising.

$$\text{RespR} = \text{span} \times (1 - e^{-\kappa l x}) \tag{7}$$

where x is the CH_4 gas concentration, κ is the effective absorption coefficient of CH_4, l is the optical path length in the gas system, which is 0.3 m for the gas cell, and *span* is a coefficient which is an indication of the amount of IR radiation that can be absorbed.

Evaluating Gas Sensor Efficacy Post-Noise Reduction. The exceptional performance of the gas sensor, assessed using stratified train samples, becomes evident with denoising parameters (wavelet type, window size, level, and threshold) specifically configured as parameters = ["sym", "10", "6", "0.4"], as shown in Figure 8a. Under this configuration, the voltage signal responses clearly show the benefits of noise reduction. Importantly, the denoised signal significantly reduces outliers, especially in areas where the CH_4 concentration is less than 10 ppm_v, effectively reducing the noticeable noise fluctuations found in the original signal. Enhanced signal resolution now supports the detection of CH_4 leaks as low as 5.6 ppm_v.

Figure 8b shows that the developed noise reduction scheme is highly effective, based on a comparative analysis of the gas sensor's reaction before and after denoising the stratified train samples. While the denoised data fits closely with the modified Beer−Lambert equation, having an R^2 value of 0.985, the original data lags with an R^2 of just 0.829. Comparing the original data to the modified Beer−Lambert equation curve shows the negative impact of noise on the initial signal, highlighting the importance of our noise reduction in enhancing signal accuracy.

Using a 95% confidence interval as depicted in Figure 8b, the uneven distribution of the confidence interval for the nondenoised data around the regression curve suggests that outliers or noise present in the original signal compromised the stability and predictive accuracy of the regression model. In contrast, the evenly distributed confidence interval postdenoising indicates that the denoising process effectively removed

https://doi.org/10.1021/acsomega.3c09769
ACS Omega 2024, 9, 19956−19967

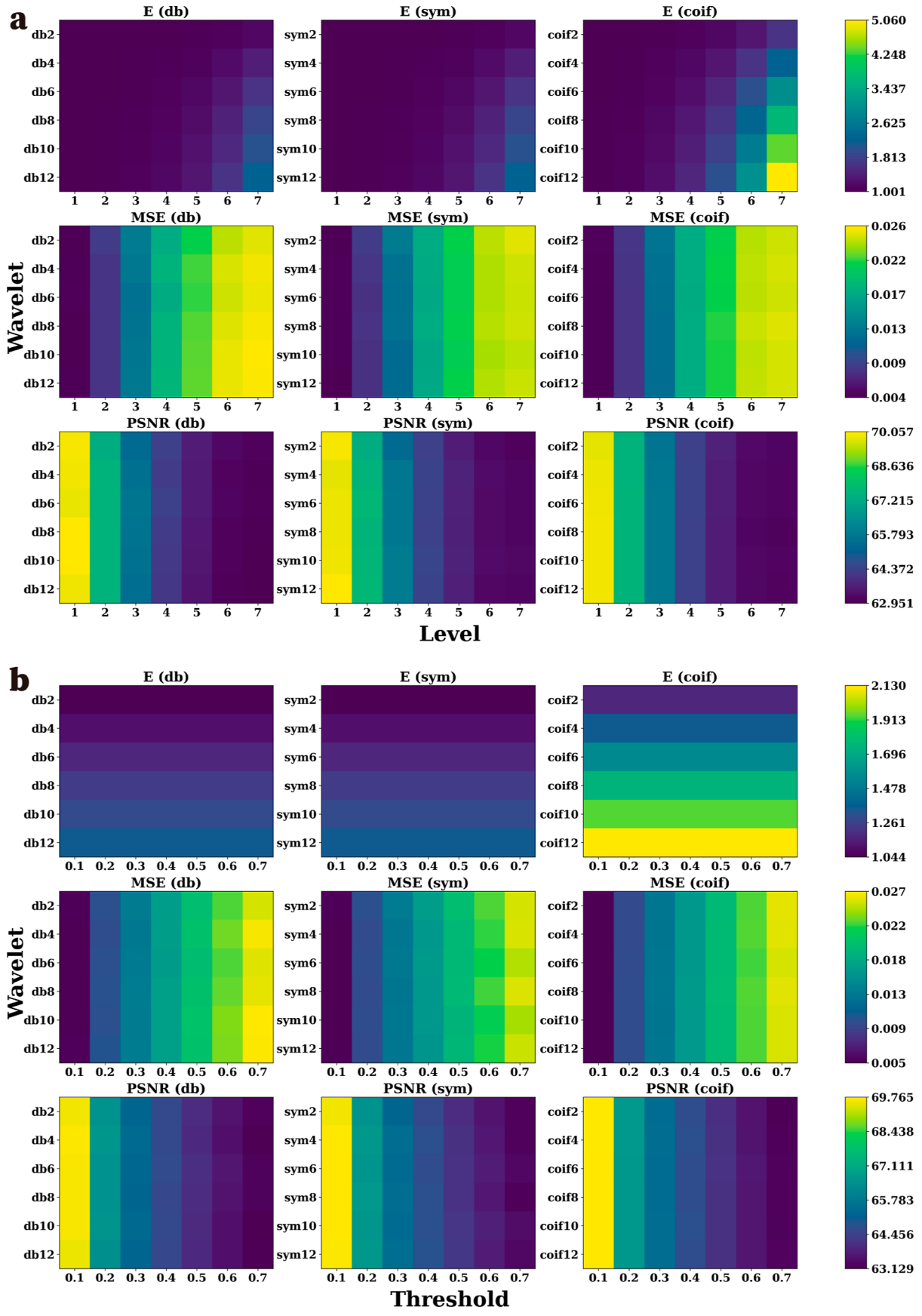

Figure 7. Analyzing wavelet denoising performance using E, MSE, and PSNR metrics. Key points include the (a) effects of wavelet levels and (b) changes brought about by threshold adjustments.

https://doi.org/10.1021/acsomega.3c09769
ACS Omega 2024, 9, 19956−19967

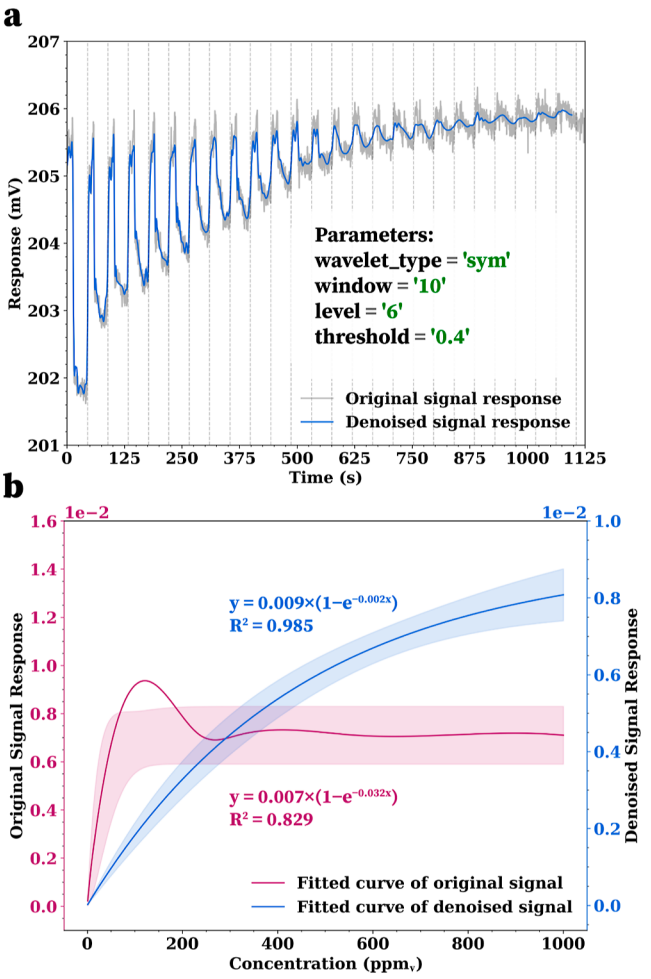

Figure 8. (a) Comparison of voltage signal responses before and after denoising. (b) Evaluation of the gas sensor's reaction to different concentrations of CH_4 within the concentration range of 1000 to 1 ppm_v.

anomalies or noise from the data, thereby enhancing the model's stability and predictive accuracy. This observation aligns with the evaluation results from the R^2 values. Notably, in areas where the CH_4 concentration is lower, the confidence interval becomes narrower, implying that the model's predictions for low-concentration CH_4 leakages will be more stable and reliable.

To further validate the robustness of our denoising algorithm, we applied stratified validation samples to observe the nonlinear regression performance under identical parameter conditions. The R^2 for the validation samples, before denoising, was only 0.77. After denoising, the result reached 0.982, closely aligning with the training samples' outcome as evidenced in Table 4, which confirms the validity of the noise reduction algorithm and parameter selections.

CONCLUSIONS

We meticulously construct an optical sensing device for CH_4 detection that features a simple yet reliable design and also consider cost effectiveness and portability in acquiring reference signals under vacuum conditions. It employs a MEMS-based pyroelectric detector operating within a spectral range of 3100−4400 nm, paired with an IR source covering an extensive wavelength range of 2 to 14 μm. The experimental design incorporates 25 dilution cycles to systematically reduce the CH_4 concentration from 1000 to 1 ppm_v in a laboratory maintained at a constant temperature of ∼26 °C. Signal response times' t_{90} value measured at CH_4 concentrations of 100.1 and 75.1 ppm_v is ∼2 and ∼2.5 s, respectively, both under 3 s, demonstrating a rapid signal response for CH_4 detection. The application of a wavelet denoising algorithm, fine-tuned through a grid search to select the optimal parameters ("sym", "10", "6", "0.4"), effectively mitigates noise and improves the limit of detection of CH_4 to 5.6 ppm_v. Based on the modified Beer−Lambert equation, the approach achieved R^2 values of 0.985 and 0.982 across different sample sets, respectively, highlighting the denoising algorithm's robustness. The novelty of our method lies in its detailed and controlled reduction of CH_4 levels, coupled with the use of wavelet denoising, which further enhances data precision and improves detection limits. Given its enhanced detection capabilities and when supplemented by the associated denoising algorithm, we believe that this approach presents a promising solution to meet the stringent requirements of early warning for CH_4 leakage on the surface at CCUS project sites. However, further validation and testing are needed to clearly establish its efficacy in diverse scenarios.

AUTHOR INFORMATION

Corresponding Authors

Wei Dong − *Department of Earth Resources Engineering, Kyushu University, Fukuoka 819-0395, Japan*; orcid.org/0009-0004-2198-0228; Email: dong.wei.454@s.kyushu-u.ac.jp

Yuichi Sugai − *Department of Earth Resources Engineering, Kyushu University, Fukuoka 819-0395, Japan*; Phone: +81 092-802-3328; Email: sugai@mine.kyushu-u.ac.jp; Fax: +81 092-802-3328

Authors

Yongjun Wang − *College of Safety Science and Engineering, Liaoning Technical University, Huludao 125105, China; Institute of Engineering and Environment, Liaoning Technical University, Huludao 125105, China*

Hemeng Zhang − *College of Safety Science and Engineering, Liaoning Technical University, Huludao 125105, China; Institute of Engineering and Environment, Liaoning Technical University, Huludao 125105, China*

Xiaoming Zhang − *Institute of Engineering and Environment, Liaoning Technical University, Huludao 125105, China*

Table 4. Evaluation of Wavelet Denoising Performance across Different Data Sets

												R^2	
type	stratified samples (ppm_v)											original	denoised
train	1000	750	562.5	316.4	237.3	13.4	10	5.6	4.2	1.8	1	0.829	0.985
val	1000	750	562.5	421.9	237.3	178	10	4.2	2.4	1.8	1	0.77	0.982

https://doi.org/10.1021/acsomega.3c09769
ACS Omega 2024, 9, 19956−19967

Kyuro Sasaki − *Institute for Future Engineering, Tokyo 135-8473, Japan*

Complete contact information is available at: https://pubs.acs.org/10.1021/acsomega.3c09769

Notes

The authors declare no competing financial interest.

■ ACKNOWLEDGMENTS

The present research was supported by MEXT/JSPS KAKENHI, grant numbers JP20H02684 and JP20K21163; CSC, grant number 202109110077; scientific research project of Education Department of Liaoning Province, grant number LJKMZ20220667.

■ REFERENCES

(1) Intergovernmental Panel on Climate Change. *Climate Change 2013—The Physical Science Basis: Working Group I Contribution to the Fifth Assessment Report of the Intergovernmental Panel on Climate Change*; Cambridge University Press: Cambridge, 2014; pp 659−740.

(2) Kirschke, S.; Bousquet, P.; Ciais, P.; Saunois, M.; Canadell, J. G.; Dlugokencky, E. J.; Bergamaschi, P.; Bergmann, D.; Blake, D. R.; Bruhwiler, L.; et al. Three Decades of Global Methane Sources and Sinks. *Nat. Geosci.* **2013**, *6*, 813−823.

(3) Howarth, R. W.; Santoro, R.; Ingraffea, A. Methane and the Greenhouse-Gas Footprint of Natural Gas from Shale Formations. *Climatic Change* **2011**, *106*, 679−690.

(4) Fletcher, S. E. M.; Schaefer, H. Rising Methane: A New Climate Challenge. *Science* **2019**, *364*, 932−933.

(5) Zhang, H.; Thanh, H. V.; Rahimi, M.; Al-Mudhafar, W. J.; Tangparitkul, S.; Zhang, T.; Dai, Z.; Ashraf, U. Improving Predictions of Shale Wettability Using Advanced Machine Learning Techniques and Nature-Inspired Methods: Implications for Carbon Capture Utilization and Storage. **2023**, *877*, 162944, .

(6) Bao, X.; Fragoso, A.; Aguilera, R. CCUS and Comparison of Oil Recovery by Huff n Puff Gas Injection Using Methane, Carbon Dioxide, Hydrogen and Rich Gas in Shale Oil Reservoirs. *SPE Canadian Energy Technology Conference and Exhibition*; 2023.

(7) Andersen, P. Ø.; Brattekås, B.; Zhou, Y.; Nadeau, P.; Nermoen, A.; Yu, Z.; Fjelde, I.; Oelkers, E. Carbon Capture Utilization and Storage (CCUS) in Tight Gas and Oil Reservoirs. *J. Nat. Gas Sci. Eng.* **2020**, *81*, 103458.

(8) Lauvaux, T.; Giron, C.; Mazzolini, M.; d'Aspremont, A.; Duren, R.; Cusworth, D.; Shindell, D.; Ciais, P. Global Assessment of Oil and Gas Methane Ultra-Emitters. *Science* **2022**, *375*, 557−561.

(9) Böttner, C.; Haeckel, M.; Schmidt, M.; Berndt, C.; Vielstädte, L.; Kutsch, J. A.; Karstens, J.; Weiß, T. Greenhouse Gas Emissions from Marine Decommissioned Hydrocarbon Wells: Leakage Detection, Monitoring and Mitigation Strategies. *Int. J. Greenh. Gas Control* **2020**, *100*, 103119.

(10) Niemann, H. B.; Atreya, S. K.; Demick, J. E.; Gautier, D.; Haberman, J. A.; Harpold, D. N.; Kasprzak, W. T.; Lunine, J. I.; Owen, T. C.; Raulin, F. Composition of Titan's Lower Atmosphere and Simple Surface Volatiles as Measured by the Cassini-Huygens Probe Gas Chromatograph Mass Spectrometer Experiment. *Int. J. Greenh. Gas Control* **2010**, *115*.

(11) Merritt, D. A.; Hayes, J. M.; Marais, D. J. D. Carbon Isotopic Analysis of Atmospheric Methane by Isotope-Ratio-Monitoring Gas Chromatography-Mass Spectrometry. *J. Geophys. Res. Atmos.* **1995**, *100*, 1317−1326.

(12) Norooz Oliaee, J.; Sabourin, N. A.; Festa-Bianchet, S. A.; Gupta, J. A.; Johnson, M. R.; Thomson, K. A.; Smallwood, G. J.; Lobo, P. Development of a Sub-Ppb Resolution Methane Sensor Using a GaSb-Based DFB Diode Laser near 3270 Nm for Fugitive Emission Measurement. *ACS Sens.* **2022**, *7*, 564−572.

(13) Xia, J.; Feng, C.; Zhu, F.; Ye, S.; Zhang, S.; Kolomenskii, A.; Wang, Q.; Dong, J.; Wang, Z.; Jin, W.; Schuessler, H. A. A Sensitive Methane Sensor of a Ppt Detection Level Using a Mid-Infrared Interband Cascade Laser and a Long-Path Multipass Cell. *Sens. Actuators, B* **2021**, *334*, 129641.

(14) Dang, J.; Kong, L.; Zheng, C.; Wang, Y.; Sun, Y.; Yu, H. An Open-Path Sensor for Simultaneous Atmospheric Pressure Detection of CO and CH_4 around 2.33 μm. *Opt Laser. Eng.* **2019**, *123*, 1−7.

(15) Xia, J.; Zhu, F.; Zhang, S.; Kolomenskii, A.; Schuessler, H. A Ppb Level Sensitive Sensor for Atmospheric Methane Detection. *Infrared Phys. Technol.* **2017**, *86*, 194−201.

(16) He, Q.; Dang, P.; Liu, Z.; Zheng, C.; Wang, Y. TDLAS−WMS Based near-Infrared Methane Sensor System Using Hollow-Core Photonic Crystal Fiber as Gas-Chamber. *Opt. Quant. Electron.* **2017**, *49*, 115.

(17) Sur, R.; Sun, K.; Jeffries, J. B.; Socha, J. G.; Hanson, R. K. Scanned-Wavelength-Modulation-Spectroscopy Sensor for CO, CO_2, CH_4 and H_2O in a High-Pressure Engineering-Scale Transport-Reactor Coal Gasifier. *Fuel* **2015**, *150*, 102−111.

(18) Li, B.; Zheng, C.; Liu, H.; He, Q.; Ye, W.; Zhang, Y.; Pan, J.; Wang, Y. Development and Measurement of a Near-Infrared CH_4 Detection System Using 1.654μm Wavelength-Modulated Diode Laser and Open Reflective Gas Sensing Probe. *Sens. Actuators, B* **2016**, *225*, 188−198.

(19) Werle, P.; Slemr, F.; Maurer, K.; Kormann, R.; Mücke, R.; Jänker, B. Near- and Mid-Infrared Laser-Optical Sensors for Gas Analysis. *Opt Laser. Eng.* **2002**, *37*, 101−114.

(20) Chen, H.; Winderlich, J.; Gerbig, C.; Hoefer, A.; Rella, C. W.; Crosson, E. R.; Van Pelt, A. D.; Steinbach, J.; Kolle, O.; Beck, V.; Daube, B. C.; Gottlieb, E. W.; Chow, V. Y.; Santoni, G. W.; Wofsy, S. C. High-Accuracy Continuous Airborne Measurements of Greenhouse Gases (CO_2 and CH_4) Using the Cavity Ring-down Spectroscopy (CRDS) Technique. *Atmos. Meas. Tech.* **2010**, *3*, 375−386.

(21) Crosson, E. A. A Cavity Ring-Down Analyzer for Measuring Atmospheric Levels of Methane, Carbon Dioxide, and Water Vapor. *Appl. Phys. B: Lasers Opt.* **2008**, *92*, 403−408.

(22) Zheng, K.; Zheng, C.; Ma, N.; Liu, Z.; Yang, Y.; Zhang, Y.; Wang, Y.; Tittel, F. K. Near-Infrared Broadband Cavity-Enhanced Spectroscopic Multigas Sensor Using a 1650 nm Light Emitting Diode. *ACS Sens.* **2019**, *4*, 1899−1908.

(23) Menduni, G.; Zifarelli, A.; Kniazeva, E.; Dello Russo, S.; Ranieri, A. C.; Ranieri, E.; Patimisco, P.; Sampaolo, A.; Giglio, M.; Manassero, F.; Dinuccio, E.; Provolo, G.; Wu, H.; Lei, D.; Spagnolo, V. Measurement of Methane, Nitrous Oxide and Ammonia in Atmosphere with a Compact Quartz-Enhanced Photoacoustic Sensor. *Sens. Actuators, B* **2023**, *375*, 132953.

(24) Triki, M.; Nguyen Ba, T.; Vicet, A. Compact Sensor for Methane Detection in the Mid Infrared Region Based on Quartz Enhanced Photoacoustic Spectroscopy. *Infrared Phys. Technol.* **2015**, *69*, 74−80.

(25) Loh, Z.; Leuning, R.; Zegelin, S.; Etheridge, D.; Bai, M.; Naylor, T.; Griffith, D. Testing Lagrangian Atmospheric Dispersion Modelling to Monitor CO_2 and CH_4 Leakage from Geosequestration. *Atmos. Environ.* **2009**, *43*, 2602−2611.

(26) Kirchgessner, D. A.; Piccot, S. D.; Chadha, A. Estimation of Methane Emissions from a Surface Coal Mine Using Open-Path FTIR Spectroscopy and Modeling Techniques. *Chemosphere* **1993**, *26*, 23−44.

(27) He, Q.; Zheng, C.; Zheng, K.; Tittel, F. K. Off-Axis Integrated Cavity Output Spectroscopy for Real-Time Methane Measurements with an Integrated Wavelength-Tunable Light Source. *Infrared Phys. Technol.* **2021**, *115*, 103705.

(28) Zheng, K.; Zheng, C.; Li, J.; Ma, N.; Liu, Z.; Zhang, Y.; Wang, Y.; Tittel, F. K. Near-Infrared Methane Sensor System Using off-Axis Integrated Cavity Output Spectroscopy with Novel Dual-Input Dual-Output Coupling Scheme for Mode Noise Suppression. *Sens. Actuators, B* **2020**, *308*, 127674.

(29) Tang, J.; Xu, Y.; Wang, G.; Etiope, G.; Han, W.; Yao, Z.; Huang, J. Microseepage of Methane to the Atmosphere from the

Dawanqi Oil-Gas Field, Tarim Basin, China. *J. Geophys. Res. Atmos.* **2017**, *122*, 4353−4363.
(30) Gong, Z.; Gao, T.; Mei, L.; Chen, K.; Chen, Y.; Zhang, B.; Peng, W.; Yu, Q. Ppb-Level Detection of Methane Based on an Optimized T-Type Photoacoustic Cell and a NIR Diode Laser. *Photoacoustics* **2021**, *21*, 100216.
(31) Ng, D. K. T.; Xu, L.; Chen, W.; Wang, H.; Gu, Z.; Chia, X. X.; Fu, Y. H.; Jaafar, N.; Ho, C. P.; Zhang, T.; Zhang, Q.; Lee, L. Y. T. Miniaturized CO_2 Gas Sensor Using 20% ScAlN-Based Pyroelectric Detector. *ACS Sens.* **2022**, *7*, 2345−2357.
(32) Ng, D. K. T.; Ho, C. P.; Xu, L.; Chen, W.; Fu, Y. H.; Zhang, T.; Siow, L. Y.; Jaafar, N.; Ng, E. J.; Gao, Y.; Cai, H.; Zhang, Q.; Lee, L. Y. T. NDIR CO_2 Gas Sensing Using CMOS Compatible MEMS ScAlN-Based Pyroelectric Detector. *Sens. Actuators, B* **2021**, *346*, 130437.
(33) Ko, K.; Lee, J.-y.; Chung, H. Highly Efficient Colorimetric CO_2 Sensors for Monitoring CO_2 Leakage from Carbon Capture and Storage Sites. *Sci. Total Environ.* **2020**, *729*, 138786.
(34) Li, Y.; Hao, J.; Song, H.; Zhang, F.; Bai, X.; Meng, X.; Zhang, H.; Wang, S.; Hu, Y.; Ye, J. Selective Light Absorber-Assisted Single Nickel Atom Catalysts for Ambient Sunlight-Driven CO_2 Methanation. *Nat. Commun.* **2019**, *10*, 2359.
(35) Kosse, P.; Kleeberg, T.; Lübken, M.; Matschullat, J.; Wichern, M. Quantifying Direct Carbon Dioxide Emissions from Wastewater Treatment Units by Nondispersive Infrared Sensor (NDIR) − A Pilot Study. *Sci. Total Environ.* **2018**, *633*, 140−144.
(36) Vincent, T. A.; Gardner, J. W. A Low Cost MEMS Based NDIR System for the Monitoring of Carbon Dioxide in Breath Analysis at Ppm Levels. *Sens. Actuators, B* **2016**, *236*, 954−964.
(37) Mannila, R.; Hyypiö, R.; Korkalainen, M.; Blomberg, M.; Kattelus, H.; Rissanen, A. Gas Detection with Microelectromechanical Fabry-Perot Interferometer Technology in Cell Phone. Next-Generation Spectroscopic Technologies VIII, 2015, pp 133−141.
(38) Barritault, P.; Brun, M.; Gidon, S.; Nicoletti, S. Mid-IR Source Based on a Free-Standing Microhotplate for Autonomous CO_2 Sensing in Indoor Applications. *Sens. Actuators, A* **2011**, *172*, 379−385.
(39) Ebermann, M.; Neumann, N.; Hiller, K.; Seifert, M.; Meinig, M.; Kurth, S. Tunable MEMS Fabry-Pérot Filters for Infrared Microspectrometers: A Review; *MOEMS and Miniaturized Systems XV*; SPIE, 2016; pp 64−83.
(40) Neumann, N.; Ebermann, M.; Kurth, S.; Hiller, K. Novel MWIR Microspectrometer Based on a Tunable Detector. *MOEMS and Miniaturized Systems* **2009**, *VIII*, 121−128.
(41) Arnold, B. C.; Beaver, R. J.; Azzalini, A.; Balakrishnan, N.; Bhaumik, A.; Dey, D. K.; Cuadras, C. M.; Sarabia, J. M.; Arnold, B. C.; Beaver, R. J. Skewed Multivariate Models Related to Hidden Truncation and/or Selective Reporting. *Test* **2002**, *11*, 7−54.
(42) Silverman, B. W. *Density Estimation for Statistics and Data Analysis*; Routledge: New York, 2017.
(43) Parzen, E. On Estimation of a Probability Density Function and Mode. *Ann. Math. Stat.* **1962**, *33*, 1065−1076.
(44) Feng, S.; Qiu, X.; Guo, G.; Zhang, E.; He, Q.; He, X.; Ma, W.; Fittschen, C.; Li, C. Palm-Sized Laser Spectrometer with High Robustness and Sensitivity for Trace Gas Detection Using a Novel Double-Layer Toroidal Cell. *Anal. Chem.* **2021**, *93*, 4552−4558.
(45) Roy, S. K.; Sauer, V. T. K.; Westwood-Bachman, J. N.; Venkatasubramanian, A.; Hiebert, W. K. Improving Mechanical Sensor Performance through Larger Damping. *Science* **2018**, *360*, No. eaar5220.
(46) Cusano, P.; Bobbio, A.; Festa, G.; Petrosino, S.; Rombetto, S. Analysis of Seismic Noise to Check the Mechanical Isolation of a Medical Device. *Ann. Geophys.* **2011**, *54*, 223−233.
(47) Lee, G. R.; Gommers, R.; Waselewski, F.; Wohlfahrt, K.; O'Leary, A. PyWavelets: A Python Package for Wavelet Analysis. *J. Open Source Softw.* **2019**, *4*, 1237.
(48) Guo, Y.; Chen, X.; Wang, W. Fault Diagnosis of Fuel Pump Based on Wavelet Denoising and Deep Learning. *J. Phys.: Conf. Ser.* **2022**, *2216*, 012050.
(49) Vilimek, D.; Kubicek, J.; Golian, M.; Jaros, R.; Kahankova, R.; Hanzlikova, P.; Barvik, D.; Krestanova, A.; Penhaker, M.; Cerny, M.; Prokop, O.; Buzga, M. Comparative Analysis of Wavelet Transform Filtering Systems for Noise Reduction in Ultrasound Images. *PLoS One* **2022**, *17*, No. e0270745.
(50) Mohamad, R.; Harun, H.; Mokhtar, M.; Adnan, W. A. W.; Dimyati, K. *Performance Analysis of Stopping Turbo Decoder Iteration Criteria*; 2014 IEEE 10th International Colloquium on Signal Processing and Its Applications, 2014; pp 5−9.
(51) Kochanov, R. V.; Gordon, I. E.; Rothman, L. S.; Wcisło, P.; Hill, C.; Wilzewski, J. S. HITRAN Application Programming Interface (HAPI): A Comprehensive Approach to Working with Spectroscopic Data. *J. Quant. Spectrosc. Radiat. Transf.* **2016**, *177*, 15−30.
(52) Tan, X.; Zhang, H.; Li, J.; Wan, H.; Guo, Q.; Zhu, H.; Liu, H.; Yi, F. Non-Dispersive Infrared Multi-Gas Sensing via Nanoantenna Integrated Narrowband Detectors. *Nat. Commun.* **2020**, *11*, 5245.

https://doi.org/10.1021/acsomega.3c09769
ACS Omega 2024, 9, 19956−19967